Crossing Thermal Lubricity and Electronic Effects in Friction: Vanadium Dioxide under the Metal–Insulator Transition

Jong Hun Kim, Deyi Fu, Sangku Kwon, Kai Liu, Junqiao Wu, and Jeong Young Park**

The remarkable turnover of friction on a vanadium dioxide (VO_2) surface driven by the metal–insulator transition is revealed using temperature-variable atomic force microscopy in ultrahigh vacuum. Phononic and electronic contributions are known as two major components in mediating friction energy dissipation. Here, a VO_2 thin film is prepared on a silicon wafer with preferential orientations of (100) and (120) in the monoclinic phase using pulsed laser deposition. Corresponding friction and conductivity images show that friction decreases below the critical temperature, above which two trends are seen as the temperature increases: less friction on the insulating domains and higher friction on the metallic domains. This distinct temperature dependence of friction is attributed to the combined effects of thermal lubricity and electronic contributions. This study indicates the promising potential for vanadium oxide to tune friction in the electric regime as well as with temperature.

1. Introduction

Friction is a natural energy-loss phenomenon that occurs when two contacting bodies slide against each other. Although it is observed in all systems, even at the atomic scale, its fundamental cause is not simple, which makes it difficult to control or to design interfaces with less wear.[1,2] From a fundamental point of view, friction—or, more precisely, mechanical energy dissipation—is the result of an interplay between basic processes (e.g., phonon generation and electron–hole pair creation); thus, determining energy dissipation mechanisms offers the potential to control friction in new ways.[3–5] Theoretically, when an object is moving along an insulator surface, kinetic energy is dissipated solely through phonon emission (i.e., lattice vibration of the substrate). However, if the substrate is conductive, electronic channels can also be activated for energy dissipation.

Friction force microscopy (FFM) enables us to investigate these issues at the nanoscale.[2,6] In FFM, the sample surface is scanned by a nanosized tip under a constant normal force while lateral distortions in the trace and retrace directions are detected, giving rise to the friction signal.[7] This provides a means to investigate how the friction force acts on the sharp tip. Indeed, FFM experiments have revealed phononic emissions dependent on the isotopic composition of the substrate[4] and electronic friction in *p–n* junctions.[5,8] Cannara et al. demonstrated that the vibration of lighter atoms could dissipate friction heat more effectively.[4] Park et al. showed that friction could be varied in a semiconductor by controlling carrier density.[6] To simultaneously demonstrate the relative magnitude of these two competing mechanisms, Kiesel utilized noncontact atomic force microscopy (AFM) and found that the superconductor state of Nb has less friction than its normal metal state[9] because friction energy cannot dissipate to paired electrons in the superconducting state until these pairs are broken apart by the friction energy itself.

Vanadium dioxide (VO_2) is a well-known material for its metal–insulator phase transition (MIT), which offers an interesting platform to study the influence of electronic structure on friction behavior. Particularly, because its transition temperature (T_c) is near room temperature (T_c = 68 °C for free-standing, stoichiometric VO_2 single crystals) and it has a high resistivity ratio and fast switching time, VO_2 attracts more attention than other materials with similar MIT characteristics.

Here, we report the role of MIT on the friction properties of VO_2 at various temperatures. FFM combined with a current preamplifier successfully resolves the metallic and insulating domains in the VO_2 by measuring its conductivity at nanoscale. We discovered that friction in the insulating phase decreases with increasing temperature, which is attributed to

Dr. J. H. Kim, Dr. S. Kwon, Prof. J. Y. Park
Center for Nanomaterials and Chemical Reactions
Institute for Basic Science (IBS)
Daejeon 305-701, Republic of Korea
Dr. J. H. Kim, Dr. S. Kwon, Prof. J. Y. Park
Graduate School of EEWS
Korea Advanced Institute of Science and Technology (KAIST)
Daejeon 305-701, Republic of Korea
E-mail: jeongypark@kaist.ac.kr
Dr. D. Fu, Dr. K. Liu, Prof. J. Wu
Department of Materials Science and Engineering
University of California
Berkeley, Berkeley, CA 94720, USA
E-mail: wuj@berkeley.edu
Dr. K. Liu, Prof. J. Wu
Materials Sciences Division
Lawrence Berkeley National Laboratory
Berkeley, CA 94720, USA

DOI: 10.1002/admi.201500388

 © 2015 WILEY-VCH Verlag GmbH & Co. KGaA, Weinheim

thermal lubricity. However, a remarkable increase in friction was observed in the metallic phase above the transition temperature, while much lower friction was measured on the neighboring insulating regions where thermal lubricity still existed.

2. Results and Discussion

To check the crystallinity of the sample, X-ray diffraction (XRD) spectroscopy was conducted using the $2\theta/\omega$ scan mode at room temperature (**Figure 1**a). Based on the XRD data, the crystallinity of the VO_2 films was mainly present along either the (200), (120), or (−120) orientations at room temperature, implying that the film was polycrystalline. Therefore, when slightly pressed with the AFM probe, the compressive force was mainly exerted to the film, thus suppressing the occurrence of the metastable insulating (M_2) phase where half of the V atoms are paired, but not twisted, as in the stable insulating (M1) phase (see the phase diagram of VO_2 in Figure S1 in the Supporting Information).

The in-plane resistance versus temperature curve for the film (Figure 1b) shows typical MIT behavior: the resistivity starts to show a slight reduction at 70 °C and then drops drastically at 75 °C with a high resistivity ratio of ρ (at 30 °C)/ρ (at 90 °C) ≈ 500. It is known that VO_2 exhibits a first-order MIT from the high-temperature metallic phase to the low-temperature insulating phase. This is accompanied by a structural change from the tetragonal structure in the metallic phase to the monoclinic structure in the insulating phase.[10]

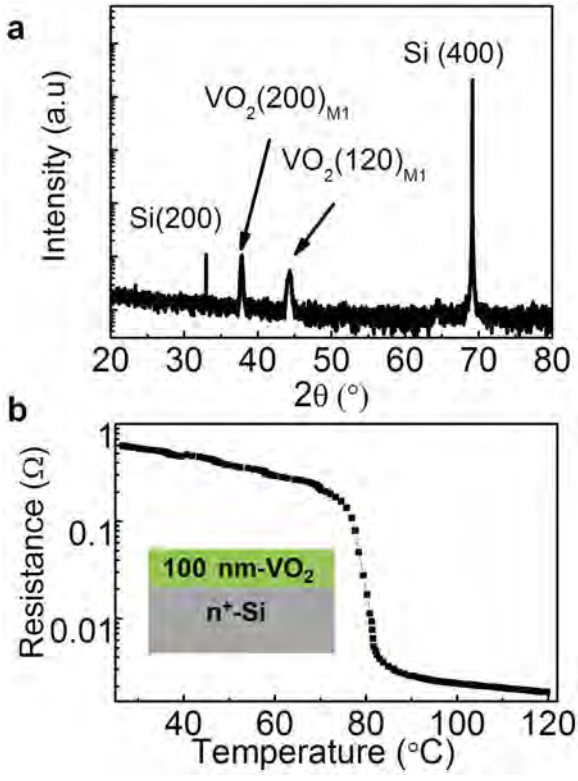

Figure 1. a) XRD of the VO_2 film. b) Resistance as a function of VO_2 thin film temperature. The inset demonstrates the structure of the VO_2 sample.

Friction and current measurements[11] were carried out under ultrahigh vacuum (UHV) with an integrated heater that varied the temperature during AFM measurements. The measurements presented here were performed in contact mode using a TiN-coated silicon cantilever and the lateral deflection difference between the trace and retrace directions is presented as friction. For a more quantitative analysis, the spring constant of the tip was calibrated based on Cleveland et al.[12] For the current measurements, the VO_2 specimen was mounted on a metallic sample holder using silver epoxy. **Figure 2**a shows the thermal evolution of the friction and current signals together with the corresponding topography as the specimen was heated from 31 to 80 °C, crossing the MIT temperature. The scan area was 200 × 200 nm^2 and the loading force was kept constant at 33 nN using a feedback loop; the current resolution was better than 5 pA. The loading force was relatively low so that neither tip wear nor sample surface scratches were detected unless the loading force was over ≈300 nN. As shown in the dark current images in Figure 2a, while there was no detectable variation of the current signal during heating to 60 °C, metallic regions suddenly appeared with bright contrast at 70 °C, covering 6% of the whole area. At 80 °C, the metallic region drastically increased up to 33% of the scanned area. The transition temperature of VO_2 is known to have a close relation to the strain such that the overlap between V^{4+} orbitals is modified by the strain.[13] As a result, the substrate with the larger thermal expansion coefficient causes the lower transition temperature of VO_2 and the observed distribution of metallic domains above T_c is ascribed to the irregular stress configuration of the VO_2 film. More exciting results occurred in the friction images. While friction on the scanned area gradually decreased as the temperature increased up to 60 °C, some sites with high friction emerged abruptly at 70 °C. To visualize the trend in friction, representative friction and current profiles at insulating (I) and metallic (M) phases are exhibited in Figure 2b. In contrast with insulating domains for which the disparity of trace and retrace friction profiles were relatively small, the difference was considerably enhanced at metal domains. We note that an asymmetric friction loop is occasionally observed, while the symmetric loop is much more common. The asymmetric friction loop is presumably related to the asymmetric geometry of the tip–sample junction such as the anisotropic coating of metal film.[14]

Because friction is proportional to loading force and loading force, in turn, is the sum of the applied load and adhesion, we need to evaluate the difference in adhesion force between the metal and insulating domains. For this purpose, the pull-off force was determined from force–distance spectroscopy of VO_2 at 80 °C that was performed at insulating and neighboring metallic domains while varying the sample bias. As shown in Figure 2c, the pull-off force showed parabolic behavior for both domains as the voltage changed; thus, we considered that the pull-off force should be affected by the capacitive force (F_{cap}), which can be formulated by the relation $F_{cap} = -1/2*V^2*\partial C/\partial z$. Here, $\partial C/\partial z$ is the derivative of the capacitance with respect to the tip–sample distance (z). Therefore, the change in the pull-off force curve toward higher curvature means the dielectric constant of the capacitance is altered to a higher value

© 2015 WILEY-VCH Verlag GmbH & Co. KGaA, Weinheim

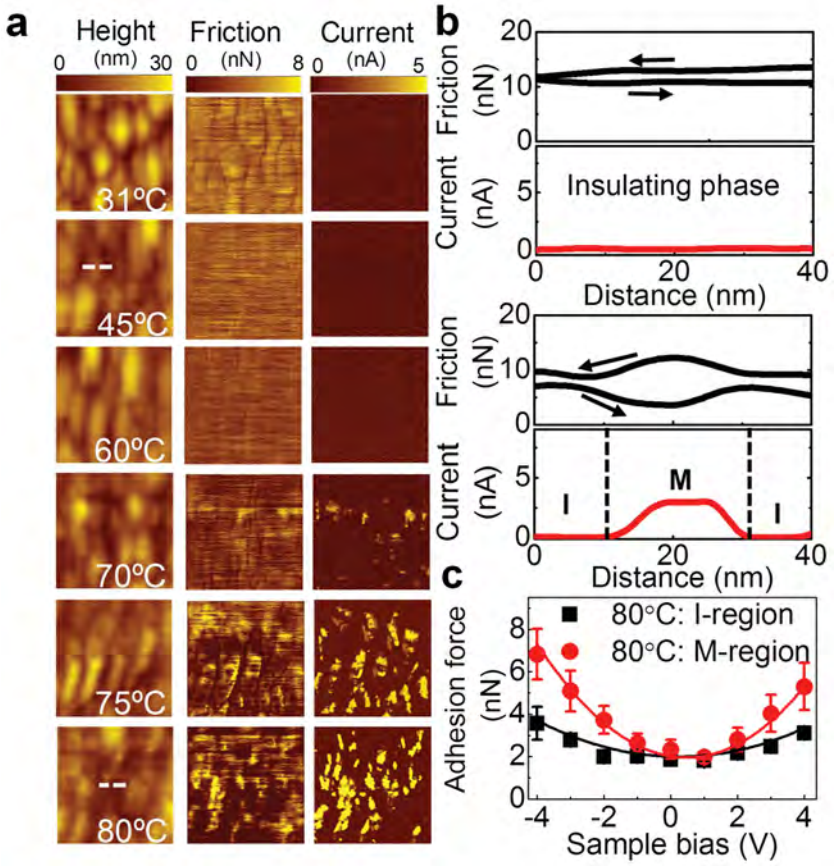

Figure 2. a) A series of 200 × 200 nm^2 height/friction/current images taken in the same region at various temperatures. The scanning rate was 0.33 s per line. b) The representative friction/current line profiles obtained at insulating (40 °C, upper curves) and metallic regions (80 °C, lower curves). Metallic (M) domains with high friction/current and insulating (I) domains with low friction/current are clearly visible. c) The adhesion force plotted as a function of sample bias on the metallic and insulating regions.

when changing to the metallic state. As a result, the adhesion increased more sharply with voltage in the metallic sites, which contributed to friction enhancement more than in insulating sites.

While morphological features can affect friction, the roughness of the metallic and insulating regions—measured while varying the sample temperature (see Figure S3 in the Supporting Information)—shows almost no distinguishable difference between the metallic and insulating regions across T_c. The topography and its profile in **Figure 3**a,b, which were measured on VO_2 at 73 °C, show that the metallic and insulating phases at different positions have a distinct difference in friction despite having almost the same height, indicating that the structure has only a limited effect on the friction. The correlation between the tribological and electrical features can be clarified more through normal load versus friction (F_n–F_f) spectroscopy, which is conducted at the metallic and insulating regions while measuring the current at the same time (Figure 3c). For F_n–F_f spectroscopy, a 20 nm line inside a grain is continuously scanned so that the effects of either the root mean squared (RMS) roughness or grain boundaries on friction are minor. This set of spectroscopy results shows that high friction coexists with high conductivity. We fit the F_n–F_f curves to the following equation

$$F_f = \mu(F_n - F_0) \quad (1)$$

where μ is the friction coefficient and F_0 is the adhesion force at zero external normal force.[15] The linear dependence between friction and applied load is associated with multiasperity contact, which comes into contact in series where only elastic deformation exists.[7] Linear fitting yields the best results when μ = 0.05 and F_0 = 6 nN for the insulating region, and μ = 0.09 and F_0 = 9 nN for the metallic region. Higher conductance on the metallic regions in Figure 3c,d supports that the higher friction region is well matched to and strongly correlates with the metallic region. However, increases in both the friction coefficient and adhesion imply that higher friction in metallic domains cannot be interpreted solely by adhesion, but that the friction on the sample surface itself was actually altered.

To understand the influence of temperature on local friction, we used F_n–F_f spectroscopy and varied the temperature from 45 to 80 °C. **Figure 4**a,b shows the load dependence of friction during the heating (increasing temperature) and cooling (decreasing temperature) processes, respectively. Again, we extracted the friction coefficients by fitting the data to Equation (1); the results are plotted as a function of temperature in Figure 4c for both the insulating and metallic regions during the heating and cooling processes. When the temperature was close to or greater than T_c, the linear friction pattern was altered to a superposition of two linear patterns and the loading force at the inflection decreased as the temperature increased (see Figure 4a,b). As shown in the phase diagram, the T_c of VO_2 is sharply sensitive to stress; local tensile stress can occur even when the loading force is decreasing. Therefore, the rapid change in friction is likely to be associated with a pressure-related transition to the insulating phase so that only the higher load was considered as the friction on the metallic domains. The downward arrows in Figure 4a,b indicate the lower limits for the fitting ranges. The fitted friction coefficient was plotted in Figure 4c as a function of the loading force. As shown in the plot, the friction coefficient of the insulating regions decreased with increasing temperature for both the heating and cooling processes. However, after the metallic region appeared at 70 °C, friction increased in this region as the temperature increased. The friction at the maximum load of 50 nN also follows similar trends, as shown in Figure S4 in the Supporting Information. Also, the trend of the friction coefficient for the heating process is quite similar to that of the cooling process, which indicates the absence of plastic deformation or irreversible changes induced by heating or cooling.

© 2015 WILEY-VCH Verlag GmbH & Co. KGaA, Weinheim

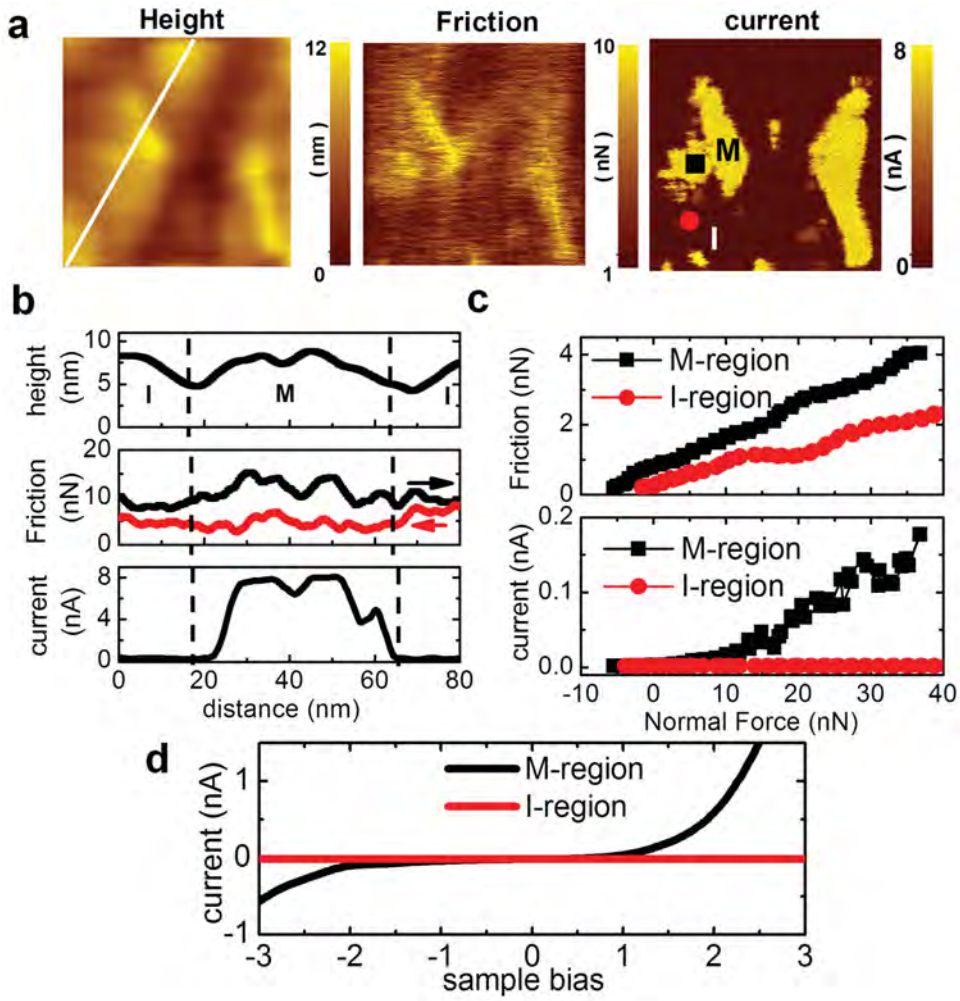

Figure 3. a) 80×80 nm^2 height/friction/current images of a region at 73 °C and b) profile of the cross section along the white line. It is clear that the height of the surface is not correlated with the friction and conductance of the surface. c) Plot of friction (upper) and current (lower) as a function of normal load on the marked points on the current map. Black squares and red circles represent metallic and insulating regions, respectively. d) Local voltage versus current curves that were obtained in the same region.

When the temperature induces tip hopping, according to Krylov and Frenken,[16] the friction is approximately proportional to $\exp\left(\frac{E_a}{k_B T}\right)$, where E_a is the potential barrier of the tip–surface system and k_B is the Boltzmann constant. To confirm this model, ln μ versus $1/T$ on the insulating region was plotted in Figure 4d for both the heating and cooling processes. The plot reveals a linear curve, leading to an activation energy of ≈0.3 eV for both the heating and cooling processes. According to Barel et al.[17] a reduction of friction during contact with a high potential barrier is preferentially caused by the rupture of bonds at the interface rather than the formation of bonds when the contact is about to slip. Therefore, as shown in Figure S5 (Supporting Information), we also checked the variation of the velocity-driven friction on an insulating region for VO_2 at 75 °C while varying the scan speed. We fitted the experimental data to Equation S1 (Supporting Information), as suggested by the literature.[18] Since the fitted parameter for maximum friction at zero temperature (F_{max}) was determined to be 0.6 nN, the energy barrier can be estimated by dividing the friction by the lattice constant (≈0.28 nm), in other words, $E \approx aF_{max}/\pi \approx$ 0.34 eV. As the energy value showed good agreement with previous results, we can safely say that the reduction in friction is due to the thermolubricity effect.

While the friction behavior on the insulating regions can be explained by a model based on thermolubricity, friction on the metallic regions shows the opposite behavior. Therefore, a mechanism other than that in the insulating state should be considered for the metallic state. Excess friction existing only in the conductive area is similar to previously reported results where a charge accumulation region exists in Si p–n junctions[5] or on n-type GaAs surfaces.[19] In these papers, forward bias conditions of ≈2.5 and ≈2 V were used, respectively, for charge accumulation. In those works, the samples were covered by a very thin oxide layer and the authors concluded that the phenomena originated from charge trapping in the top dielectric layer.[5,8,19] Since this dielectric layer readily forms on the VO_2 film in our study as well, we attribute it to

© 2015 WILEY-VCH Verlag GmbH & Co. KGaA, Weinheim

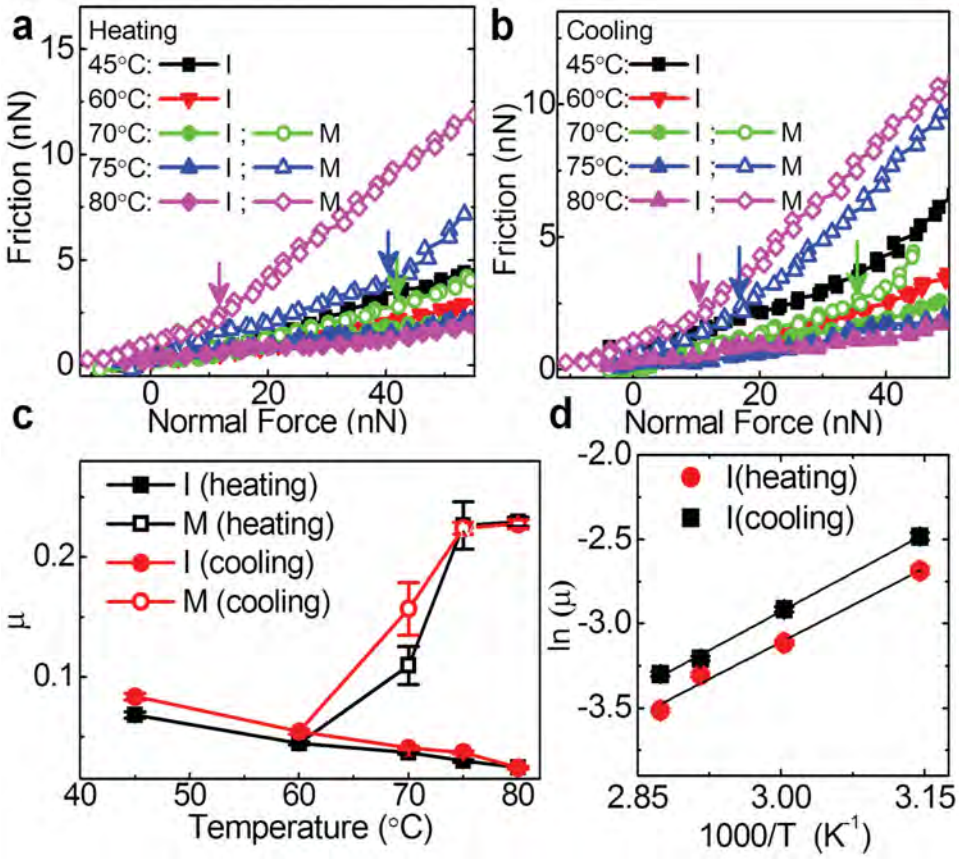

Figure 4. Normal force versus friction plots measured during the a) heating and b) cooling phases. c) Friction slopes obtained from (a) and (b). In the metallic range, the fitting range for the friction coefficient is limited and the downward arrows indicate the lowest values of the linear fitting range. d) Friction slopes of the I sites in (c) are redrawn in the Arrhenius form of ln μ versus $1/T$. The linear behavior shows that with the increased bond-rupturing rate, the kinetic friction force decreased at high temperature.

V_2O_5, whose presence was confirmed via X-ray photoelectron spectroscopy (XPS) (see Figure S6 in the Supporting Information). Considering the fact that both V_2O_5 and the underlying VO_2 are observed together within the inelastic mean free path of an electron in the XPS, we believe that V_2O_5 with a thickness of only several nm exists on the surface. Contrary to VO_2 or V_2O_3, V_2O_5 is known to be an insulator even at higher temperatures (above 250 °C) and has a band gap as large as 2.4 eV.[20] Additionally, several previous works reportboth theoretically and empirically that spontaneous surface oxidation of VO_2 to V_2O_5 is thermodynamically favorable.[21] Therefore, the charge-trapping effect of V_2O_5 is enhanced at temperatures above the T_c of VO_2 where almost all of the electric field is applied to the insulating V_2O_5 layer rather than to the metallic VO_2. We assume that the tip leaves a trace of trapped charges as it scans the sample surface, as shown in the scheme in Figure S7a (Supporting Information). Subsequently, if the friction is equivalent to the excess friction gained from Coulomb forces between the tip and the surface, the Coulomb forces can be estimated using the following linear charge-trapping model

$$F_{\text{coulmb}} = \int_0^L ne\sigma e / \left[4\pi K\varepsilon_0 \left(x^2 + d^2\right)\right] x / \sqrt{x^2 + d^2}\, \mathrm{d}x \qquad (2)$$

as shown in Qi et al.[19] Here, L is the lateral distribution length of the trapped charges, e is the electric charge, n is the number density of charges, σ is the trap density along the scan direction, and x is the lateral position of an arbitrary charge in the V_2O_5. K and ε_0 represent the dielectric constants of V_2O_5 (37) and a vacuum, respectively. Based on the fact that both V_2O_5 and the underlying VO_2 are observed together in the XPS, the thickness of V_2O_5 is assumed to be comparable to the inelastic mean free path, ≈2 nm.[22] Therefore, if the trap depth is located in the middle, the distance between the tip charge and the trap charge (d) is ≈2 nm. The areal density of the trapped charges is assumed to be on the order of 10^{13} cm^{-2}, which is reasonable when compared to values reported in other experiments where AFM was utilized to measure charge trapping for Si_3N_4/SiO_2 and SiO_2/GaAs. Based on the electrostatic force microscopy results where the trap/detrap time of a single charge in VO_2 at room temperature was reported to be greater than 1 s,[23] we can suppose that the relaxation time of V_2O_5 is also greater than 1 s because the energy gap of V_2O_5 is wider than that of VO_2. As shown in Figure S7b (Supporting Information), to calculate the contact area of the tip, we fitted the F_n–F_f spectrum results for the metallic regions in Figure 3c to the Derjaguin–Müller–Toporov model where the friction force can be found by multiplying the contact area by the shear

© 2015 WILEY-VCH Verlag GmbH & Co. KGaA, Weinheim

strength.[24] The best fit was achieved with a shear strength of ≈370 MPa and contact area of 9 nm^2 at a loading force of 33 nN. Therefore, the diameter of the contact area can be calculated to be ≈3.5 nm at 33 nN, leading to $\sigma \approx 0.3e$ trapped per nanometer along the fast scan direction. On the other hand, the induced charge on the tip can be the sum of the image charge for the charges trapped on the sample surface and the charge induced by the sample bias. The first term is on the order of σL (i.e., the scan velocity of 670 nm s^{-1}) multiplied by the life time (≈1 s) so that the number of image charges for the unrelaxed charge on the sample is ≈180e. Meanwhile, when using a parallel capacitor model, the bias-induced charge can be simply calculated by the capacitance of 2 nm V_2O_5 multiplied by voltage. Thereby, a 0.5 V bias will induce ≈7e for the tip contact area and the total charge of the tip will amount to ≈190e. This calculation leads to a Coulomb force of ≈5 nN between the tip and the V_2O_5. Considering the friction differences between the metal and insulator in Figures 2b and 3b,c, the increased force has the same order of magnitude as the measured results. Since the applied voltage is predominantly focused on the thin V_2O_5 layer rather than on the metallic VO_2, this charge-trapping effect can be pronounced. Besides, as Wu et al.[23] exhibited, the trapping/detrapping of charges could occur on the surface of a vanadium oxide thin film even when the tip is placed in the noncontact regime and the relaxation time of the trapped charge is on the order of seconds; thus, our charge-trapping-induced friction hypothesis during conductive AFM is reasonable.

On the other hand, the presence of V_2O_5 can be attributed to increased adhesion, as mentioned, due to its dielectric constant being higher than that of VO_2, as shown in Figure 2c. According to the literature, the capacitance force between the spherical conductive tip and the flat sample, $F_{cap} = -1/2^*V^{2*}\partial C/\partial z$, can be assessed by using the following equation[25]

$$C(R,z) \cong 4\pi\varepsilon_0 R \sinh\left(\frac{z+R}{R}\right) \times \sum_{n=1}^{n=\infty}\left(\frac{K-1}{K+1}\right)^{n-1} \operatorname{csch}\left(\frac{n(z+R)}{R}\right) \quad (3)$$

where R is the tip radius, z is the distance between the tip and the sample (≈1 nm), and K is the dielectric constant of the sample. Thus, we calculated F_{cap} at the conditions of $R = 20$ nm, $z = 1$ nm, and $K = 20$ (for VO_2) or $K = 37$ (for V_2O_5). The difference between the calculated capacitance of $K = 20$ and $K = 37$ is then plotted as a function of voltage in order to match the experimental data for the metallic state in Figure 2c. Figure S8 (Supporting Information) shows that the measured adhesion behavior can be interpreted by the capacitance force model. For a better match, we displaced the calculated plot by 0.6 V, which is thought to originate from the difference in work functions between the TiN tip (≈4.6 eV[26]) and the sample work function (–5.15 eV[27]). Therefore, we can attribute the increased curvature of the adhesion data on the metallic domains in Figure 2c to the higher capacitance of V_2O_5 compared with that of VO_2. Both of the coulomb interactions due to charge trapping and capacitive force are attractive; thus, both of them are expected to contribute to increased friction. However, when VO_2 turns into an insulator, the voltage is applied nearly overall to the 100 nm VO_2 so that the electrical field should be rapidly lowered by more than an order of magnitude and the charge trapping effect can be ignored as well. Here, the screening length of VO_2 in the insulating state is assumed to be negligible compared with the sample thickness. In practice, other possible models (e.g., electron–hole pair creation, electron wind, charge carrier dragging, and fluctuation of the electric field) have such small dissipation parameters that they are not likely to be responsible for the large enhancement of friction observed on the metallic VO_2. The observed combined effect of phonons and electrons in friction can give rise to the intriguing possibility of controlling nanoscale friction. Similar to Park et al.[5,8] and Qi et al.,[19] the velocity dependence of friction on single-crystal VO_2 with larger domains can be the subject of further investigation.

3. Conclusion

In conclusion, we report a remarkable phenomenon of friction energy mediated by phononic and electronic effects by probing the local friction properties of a VO_2 film at various temperatures around T_c. While the friction decreased with increasing temperature below T_c, the trend is divided into two types determined by the electrical resistivity above T_c: decreasing friction with increasing temperature on insulating regions, and a sharp increase in friction with increasing temperature on metallic regions. Thermal hopping of the tip is thought to be a reason for lower friction on the insulating phase. Based on the fact that both the friction and adhesion forces increase when entering the metallic phase, the friction surge at the metallic sites can be caused by both capacitive force and Coulomb attraction from trapped charges. For Coulomb attraction, the surface V_2O_5 dielectric layer is proposed to work as a charge-trapping layer that yields excess friction when the temperature is greater than T_c. At the moment, it is not clear whether the trapped charges came from the tip or from the substrate. Therefore, a study of the hysteresis curve from either capacitance versus voltage or current versus voltage is necessary to find the precise pathway for charge trapping.

4. Experimental Section

Sample Preparation: A 100 nm thick VO_2 film was prepared on a heavily doped n-type Si substrate by pulsed laser deposition. The growth details can be found elsewhere.[28] A KrF excimer laser ($\lambda = 248$ nm) was focused onto a target (pressed 99.9% pure VO_2 powder with density of ≈4.0 g cm^{-3}) with a fluence of ≈1.3 J cm^{-2}. The deposition chamber was pumped down to ≈10^{-6} Torr before oxygen gas was introduced into the chamber. The deposition was performed in 10 mTorr oxygen with the substrate temperature maintained at 520 °C for 40 min. After deposition, the samples were cooled at a rate of 10 °C min^{-1} at the same oxygen pressure. The typical RMS value of the surface roughness was 5.7 nm, as measured using AFM.

High-Resolution X-Ray Diffraction: The crystallinity of the films at room temperature was measured using high-resolution XRD, which was performed using a triple-axis diffractometer equipped with a four-crystal Ge (220) monochromator and a three-reflection Ge (220) analyzer in a PANalytical X'Pert Pro MRD system. The Cu Kα line ($\lambda = 0.15406$ nm) radiated from a 2.2 kW ceramic tube was used as the X-ray source. Two well-resolved diffraction peaks were observed from monoclinic VO_2 (i.e., $VO_2(200)_{M1}$ and $VO_2(120)_{M1}$ peaks; Figure 1a), which corresponded to the two preferred crystal orientations of these polycrystalline films. For

© 2015 WILEY-VCH Verlag GmbH & Co. KGaA, Weinheim

both orientations, the c_R axis (*c* axis in the metallic phase) was slightly tilted from the film growth direction.

AFM Measurement: For the AFM measurements, an RHK Tech SPM100 AFM system was used and all of the measurements were carried out at 1.0×10^{-9} Torr. The vacuum was of great importance because it not only removed the capillary forces caused by water in ambient environments, but also protected the tip from oxidation during current measurements. The spring constant of the tip was calibrated using its geometry and the resonance frequency in its free state.[12] The resonance frequency of the tip was measured and the geometry of the tip was checked with a scanning electron microscopy image and the provided factory specifications. For F_n–F_f spectroscopy, the tip continuously scanned only a single line inside the grain while decreasing the external normal loading force until the tip completely disengaged from the surface. To precisely determine the elastic constant of the tip, the method of Cleveland et al. was followed where the elastic constant (k) of a rectangular probe can be defined as $k = 2\pi^3\beta^3 w\rho^{1.5}E^{-0.5}\upsilon_0^3$.[12] Here, the length ($l$) and width ($w$) of the cantilever were checked using scanning electron microscopy and the elastic modulus (E) and the density (ρ) are defined by the factory-provided specifications. υ_0 is the resonance frequency of the tip at the freestanding state. During the scanning process, the motion along the slow-scan direction was fixed so that only a single line was repeatedly scanned. While the loading force was changed on a line-by-line basis, differences between the forward and backward lateral signals were recorded 256 times at every step of the loading force. Therefore, the friction force for each loading force was calculated by averaging each data set (i.e., 256 measurements). To convert the lateral signal to friction force, a thermally grown 500 nm SiO_2 wafer was used as a calibration sample for the F_n–F_f spectroscopy test. As shown in Figure S2 (Supporting Information), the gradient of the friction signal was linear over the measured regime. Therefore, the slope was matched to the known friction coefficient of SiO_2 under UHV conditions (i.e., 0.4) to convert the lateral signal to the friction force (nN). Meanwhile, the contrast in the friction and current maps in Figure 2 was adjusted so as to use an identical intensity scale within the entire measured temperature range. The scanning velocity was fixed at 670 nm s^{-1}. Once a location for F_n–F_L spectroscopy was decided upon in the current map, both friction and current were measured at the same time while spectroscopy with a 20 nm scan line ran inside the area (≈50 nm scale) with a sample bias of 0.5 V. By plotting the current as a function of normal force, the validity of the spectroscopy could be confirmed by checking the variation of the current.

Supporting Information

Supporting Information is available from the Wiley Online Library or from the author.

Acknowledgements

This work was supported by IBS-R004-G4. The work at UC Berkeley and the Lawrence Berkeley National Laboratory was supported by the NSF Center for Energy Efficient Electronics Science (NSF Award No. ECCS-0939514).

Received: July 18, 2015
Revised: October 13, 2015
Published online: November 17, 2015

[1] a) E. Gnecco, E. Meyer, *Fundamentals of Friction and Wear on the Nanoscale*, Springer, Berlin, **2007**; b) B. N. J. Persson, *Sliding Friction: Physical Principles and Applications*, Springer, Berlin, **2000**.

[2] M. Urbakh, E. Meyer, *Nat. Mater.* **2010**, *9*, 8.

[3] A. Dayo, W. Alnasrallah, J. Krim, *Phys. Rev. Lett.* **1998**, *80*, 1690.

[4] R. J. Cannara, M. J. Brukman, K. Cimatu, A. V. Sumant, S. Baldelli, R. W. Carpick, *Science* **2007**, *318*, 780.

[5] J. Y. Park, D. F. Ogletree, P. A. Thiel, M. Salmeron, *Science* **2006**, *313*, 186.

[6] J. Y. Park, D. F. Ogletree, M. Salmeron, R. A. Ribeiro, P. C. Canfield, C. J. Jenks, P. A. Thiel, *Science* **2005**, *309*, 1354.

[7] J. Y. Park, M. Salmeron, *Chem. Rev.* **2013**, *114*, 677.

[8] J. Y. Park, Y. B. Qi, D. F. Ogletree, P. A. Thiel, M. Salmeron, *Phys. Rev. B* **2007**, *76*, 064108.

[9] M. Kisiel, E. Gnecco, U. Gysin, L. Marot, S. Rast, E. Meyer, *Nat. Mater.* **2011**, *10*, 119.

[10] a) J. Cao, Y. Gu, W. Fan, L. Q. Chen, D. F. Ogletree, K. Chen, N. Tamura, M. Kunz, C. Barrett, J. Seidel, J. Wu, *Nano Lett.* **2010**, *10*, 2667; b) J. Cao, E. Ertekin, V. Srinivasan, W. Fan, S. Huang, H. Zheng, J. W. L. Yim, D. R. Khanal, D. F. Ogletree, J. C. Grossmanan, J. Wu, *Nat. Nanotechnol.* **2009**, *4*, 732.

[11] J. Y. Park, S. Maier, B. Hendriksen, M. Salmeron, *Mater. Today* **2010**, *13*, 37.

[12] J. P. Cleveland, S. Manne, D. Bocek, P. K. Hansma, *Rev. Sci. Instrum.* **1993**, *64*, 403.

[13] J. Sakai, M. Zaghrioui, M. Matsushima, H. Funakubo, K. Okimura, *J. Appl. Phys.* **2014**, *116*, 123510.

[14] J. W. Li, C. Wang, G. Y. Shang, Q. M. Xu, Z. Lin, J. J. Guan, C. L. Bai, *Langmuir* **1999**, *15*, 7662.

[15] a) E. Riedo, H. Brune, *Appl. Phys. Lett.* **2003**, *83*, 1986; b) A. D. Corwin, M. P. de Boer, *Appl. Phys. Lett.* **2004**, *84*, 2451; c) A. Schirmeisen, L. Jansen, H. Holscher, H. Fuchs, *Appl. Phys. Lett.* **2006**, *88*, 123108.

[16] S. Y. Krylov, J. W. M. Frenken, *Phys. Status Solidi B* **2014**, *251*, 711.

[17] a) I. Barel, M. Urbakh, L. Jansen, A. Schirmeisen, *Phys. Rev. Lett.* **2010**, *104*, 064104; b) I. Barel, M. Urbakh, L. Jansen, A. Schirmeisen, *Tribol. Lett.* **2010**, *39*, 311.

[18] a) A. Socoliuc, R. Bennewitz, E. Gnecco, E. Meyer, *Phys. Rev. Lett.* **2004**, *92*, 134301; b) E. Riedo, E. Gnecco, R. Bennewitz, E. Meyer, H. Brune, *Phys. Rev. Lett.* **2003**, *91*, 084502.

[19] Y. B. Qi, J. Y. Park, B. L. M. Hendriksen, D. F. Ogletree, M. Salmeron, *Phys. Rev. B* **2008**, *77*, 184105.

[20] a) M. Kang, I. Kim, S. W. Kim, J. W. Ryu, H. Y. Park, *Appl. Phys. Lett.* **2011**, *98*, 131907; b) C. R. Aita, Y. L. Liu, M. L. Kao, S. D. Hansen, *J. Appl. Phys.* **1986**, *60*, 749; c) Z. S. El Mandouh, M. S. Selim, *Thin Solid Films* **2000**, *371*, 259.

[21] a) T. A. Mellan, R. Grau-Crespo, *J. Chem. Phys.* **2012**, *137*, 154706; b) T. D. Manning, I. P. Parkin, M. E. Pemble, D. Sheel, D. Vernardou, *Chem. Mater.* **2004**, *16*, 744.

[22] G. G. Fuentes, E. Elizalde, F. Yubero, J. M. Sanz, *Surf. Interface Anal.* **2002**, *33*, 230.

[23] B. Wu, A. Zimmers, H. Aubin, R. Ghosh, Y. Liu, R. Lopez, *Phys. Rev. B* **2011**, *84*, 241410.

[24] M. Enachescu, R. J. A. van den Oetelaar, R. W. Carpick, D. F. Ogletree, C. F. J. Flipse, M. Salmeron, *Phys. Rev. Lett.* **1998**, *81*, 1877.

[25] a) W. Smythe, *Static and Dynamic Electricity*. McGraw-Hill, London, **1950**, 582; b) D. Sarid, *Scanning Force Microscopy*, Oxford University Press, New York, **1991**.

[26] T. Matsukawa, Y. X. Liu, K. Endo, J. Tsukada, H. Yamauchi, Y. Ishikawa, S. O'uchi, W. Mizubayashi, H. Ota, S. Migita, Y. Morita, M. Masahara, *Jpn. J. Appl. Phys.* **2014**, *53*, 04EC11.

[27] G. Teran-Escobar, J. Pampel, J. M. Caicedo, M. Lira-Cantu, *Energy Environ. Sci.* **2013**, *6*, 3088.

[28] D. Y. Fu, K. Liu, T. Tao, K. Lo, C. Cheng, B. Liu, R. Zhang, H. A. Bechtel, J. Q. Wu, *J. Appl. Phys.* **2013**, *113*, 043707.

 © 2015 WILEY-VCH Verlag GmbH & Co. KGaA, Weinheim